Frontiers of Optoelectronics (2022) 15:36
https://doi.org/10.1007/s12200-022-00040-5

Frontiers of Optoelectronics

RESEARCH ARTICLE

Fabrication and characterization of ZnO/$Se_{1-x}Te_x$ solar cells

Jiajia Zheng[1,2] · Liuchong Fu[1] · Yuming He[1] · Kanghua Li[1] · Yue Lu[1,2] · Jiayou Xue[1,2] · Yuxuan Liu[1] · Chong Dong[1] · Chao Chen[1] · Jiang Tang[1,2]

Received: 26 April 2022 / Accepted: 26 June 2022

Abstract
Selenium (Se) element is a promising light-harvesting material for solar cells because of the large absorption coefficient and prominent photoconductivity. However, the efficiency of Se solar cells has been stagnated for a long time owing to the suboptimal bandgap (> 1.8 eV) and the lack of a proper electron transport layer. In this work, we tune the bandgap of the absorber to the optimal value of Shockley–Queisser limit (1.36 eV) by alloying 30% Te with 70% Se. Simultaneously, ZnO electron transport layer is selected because of the proper band alignment, and the mild reaction at ZnO/$Se_{0.7}Te_{0.3}$ interface guarantees a good-quality heterojunction. Finally, a superior efficiency of 1.85% is achieved on ZnO/$Se_{0.7}Te_{0.3}$ solar cells.

Keywords $Se_{1-x}Te_x$ alloy · ZnO electron transport layer · Recombination mechanism · Solar cells

1 Introduction

Selenium (Se) is the oldest photovoltaic (PV) semiconductor material [1] with a bandgap (E_g) of 1.8–2.0 eV [2, 3], a large absorption coefficient (> 10^4 cm^{-1}) at visible spectrum [4], and a theoretical Shockley–Queisser (S–Q) limit beyond 20% [5, 6]. Compared with $Cu_2(In,Ga)(S,Se)_2$ [7], organic–inorganic hybrid halide perovskites [8–10] and CdTe [11] photovoltaic materials, Se has the advantages of easy phase control, good air stability and nontoxicity. Meanwhile, benefitting from the low melting point (221 °C) and high vapor pressure (1.1 Pa @250 °C) [12], Se film can be prepared at low temperature by vacuum technologies on various substrates [13–17], showcasing a great potential for large-scale production.

Se solar cells, based on indium tin oxide (ITO)/TiO_2/Se/Au device structure, reached an impressive efficiency of 5% in 1985 [15], but the progress was slow for the following 30 years [16, 18–20]. Si advanced so rapidly that Se has not received much attention for a long time [21, 22]. Until 2017, Todorov et al. created a record efficiency of 6.5% by optimizing the functional layer thickness and adopting a MoO_x hole transport layer [17]. It is notable that the bandgap of Se is out of the optimal range of S–Q limit (1–1.5 eV), so it would lead to an inadequate use of sunlight and thereby a low photocurrent. Tellurium (Te), as the congener of Se, has a narrow bandgap of 0.33 eV [23] and the same hexagonal crystal structure [24], thus, it is possible to continuously tune the bandgap of $Se_{1-x}Te_x$ to the optimal S–Q bandgap of 1.36 eV. Se and Te are two less-studied photovoltaic materials and stand out for their simple composition, high carrier mobility, good air stability, high photoconductivity and thermoelectric response [25, 26]. They are also the significant components of transition metal dichalcogenides (TMDCs), which are widely applied in high-performance field-effect transistors (FETs) [27, 28], optoelectronic devices [29], and thermoelectric devices.

Owing to the tunable photoconductivity and optical response of $Se_{1-x}Te_x$, it has been used for solar cells [30], short-wave infrared photodetectors [31] and semiconductor core optical fibers [32]. In 2019, Hadar et al. investigated $Se_{1-x}Te_x$ films for PV application [30], but the efficiency of the alloy solar cells is less than 3%, only half of the pure Se solar cells. Therefore, it is important to choose the $Se_{1-x}Te_x$ film with a suitable component and bandgap. In addition, the current Se and $Se_{1-x}Te_x$ solar cells commonly adopt TiO_2 as an electron transport layer (ETL) [15, 16, 20]. Unfortunately

✉ Chao Chen
cchen@mail.hust.edu.cn

[1] Wuhan National Laboratory for Optoelectronics (WNLO) and School of Optical and Electronic Information, Huazhong University of Science and Technology, Wuhan 430074, China

[2] China-EU Institute for Clean and Renewable Energy (ICARE), Huazhong University of Science and Technology, Wuhan 430074, China

Published online: 08 September 2022

the inertness of TiO_2 surface cannot be bonded with $Se_{1-x}Te_x$ tightly and may potentially give rise to an inferior interface with poor adhesion. ZnO surface is more reactive than TiO_2, and ZnO has a higher electron mobility (> 150 $cm^2/(V{\cdot}s)$) [33] and lower fabrication temperature [34]. Therefore, ZnO is a preferred alternative compared to TiO_2.

In this work, we optimized the component and bandgap of $Se_{1-x}Te_x$ absorber and adopted the active ZnO ETL to assemble solar cell devices. First, we alloyed Se films with Te at certain molar ratios (x = [Te] = 0.2, 0.3, 0.4, 0.5) and tuned the bandgap from 1.53 to 1.13 eV. Based on the S–Q limit, we chose the $Se_{0.7}Te_{0.3}$ film with a bandgap of 1.36 eV for the target absorber material. Then, combining the band alignment and surface reactivity, ZnO ETL was selected to construct ITO/ZnO/$Se_{1-x}Te_x$/Au solar cells. Factually, theoretical thermodynamic calculation confirmed that ZnO can react with Se, and the Zn^{2+} exposed at (111) polar surface of ZnO fabricated by magnetron sputtering under oxygen-poor condition (O:Ar = 1:99) is more conducive to the formation of Zn-Se bonds at the ZnO/Se interface. Therefore, it can help to form a strong-adhesion interface and obtain satisfactory device performance. Finally, we achieved a superior efficiency of 1.85% on ITO/ZnO/$Se_{0.7}Te_{0.3}$/Au solar cell.

2 Experimental section

2.1 Film and device preparation

For the preparation of $Se_{1-x}Te_x$ raw materials, a certain proportion (x = [Te] = 0.2, 0.3, 0.4, 0.5) of Se and Te powder (99.999% purity, Aladdin) were sealed in a quartz tube, then heated at 560 °C in a muffle furnace for 24 h, and slowly cooled to room temperature with a cooling rate of 22 °C/h. For device preparation, the ITO glass (Kaivo, Zhuhai, China) with the square resistance of 6–8 Ω/sq was used as the substrate. The ITO substrates had been cleaned using a detergent, isopropanol, ethyl alcohol and DI water rinsing in sequence. Then 1 μm $Se_{1-x}Te_x$ films were deposited by thermal evaporation (Kurt J. Lesker, ~ 5×10^{-3} Pa), and annealed at 200 °C for 2 min on a heating stage in the glove box. Subsequently, ZnO films (180 nm thickness) were prepared by magnetron sputtering (JCP500, Technol Science; O:Ar = 1:99 atmosphere). Finally, Au electrodes (0.09 cm^2 area, 100 nm thickness) were evaporated by the resistance evaporation thin-film system (Beijing Technol Science) under a vacuum pressure of 5×10^{-3} Pa.

2.2 Film characterization

The morphologies and energy dispersive spectroscopy (EDS) characterization of $Se_{0.7}Te_{0.3}$ films were checked by scanning electron microscopy (SEM, GeminiSEM, Zeiss, without Pt coating). The X-ray diffraction (XRD) with Cu Kα radiation (Empyrean, PANalytical B.V.) was carried out to determine the component and orientation of $Se_{0.7}Te_{0.3}$ and ZnO films. The morphologies of the $Se_{1-x}Te_x$ and ZnO films were observed by the atomic force microscope (AFM, SPM9700, Shimadzu). The optical transmittance of $Se_{1-x}Te_x$ film was recorded by UV–Vis spectrophotometer (Perkin Elmer Instruments, Lambda 950 using integrating sphere). Ultraviolet photoelectron spectroscopy (UPS, AXIS-ULTRA DLD-600 W, Kratos) was used to confirm the energy level positions of $Se_{0.7}Te_{0.3}$. The Hall coefficient and carrier concentration were obtained via a Hall measurement system (Ecopia HMS5500). The X-ray photoelectron spectroscopy (XPS, AXIS-ULTRA DLD-600 W) was used to characterize the interface between $Se_{1-x}Te_x$ and ZnO).

2.3 Device characterization

The device performance was characterized by a digital source meter (Keithley2400) under simulated AM 1.5G solar (Oriel 94023A, light intensity of 1000 mW/cm^2 calibrated with a standard silicon cell). external quantum efficiency (EQE) measurements were carried out using a 300 W xenon lamp of Newport (Oriel, 69911) as a light source and a Newport oriel cornerstone TM 130 1/8 Monochromator (Oriel, model 74004) to split light into monochromatic waves. Capacitance–voltage (*C–V*) and drive-level capacitance profiling (DLCP) measurement was carried out with Keithley 4200-CVU module at a frequency of 70 kHz. Temperature dependent admittance spectral (AS, Agilent E4980A LCR meter) was used for temperature-dependent AS and conductivity measurements, and samples were put in a liquid nitrogen cryostat (Janis VPF-100). The temperature was controlled by a temperature controller (Lakeshore 325) and ranged from 80 to 320 K at a step of 10 K. When the setting temperature was stable, AS and current–voltage (*I–V*) measurements were performed using an impedance analyzer (Agilent E4980A LCR meter) and a semiconductor device parameter analyzer (Agilent B1500A), respectively.

3 Results and discussion

A certain proportion of Se and Te powder were mixed evenly to form $Se_{1-x}Te_x$ (x = 0.2, 0.3, 0.4, 0.5) blocks (Additional file 1: Fig. S1). Then the $Se_{1-x}Te_x$ films were deposited at room temperature by thermal evaporation (Fig. 1a) using $Se_{1-x}Te_x$ powder ground from the blocks. The as-deposited films were amorphous (Additional file 1: Fig. S2a), so a post-annealing process was required. The film with intermediate component x = [Te] = 0.3 was selected to study the annealing temperature from 150 to 250 °C. The film annealed at 250 °C for 2 min was thermally decomposed because of the

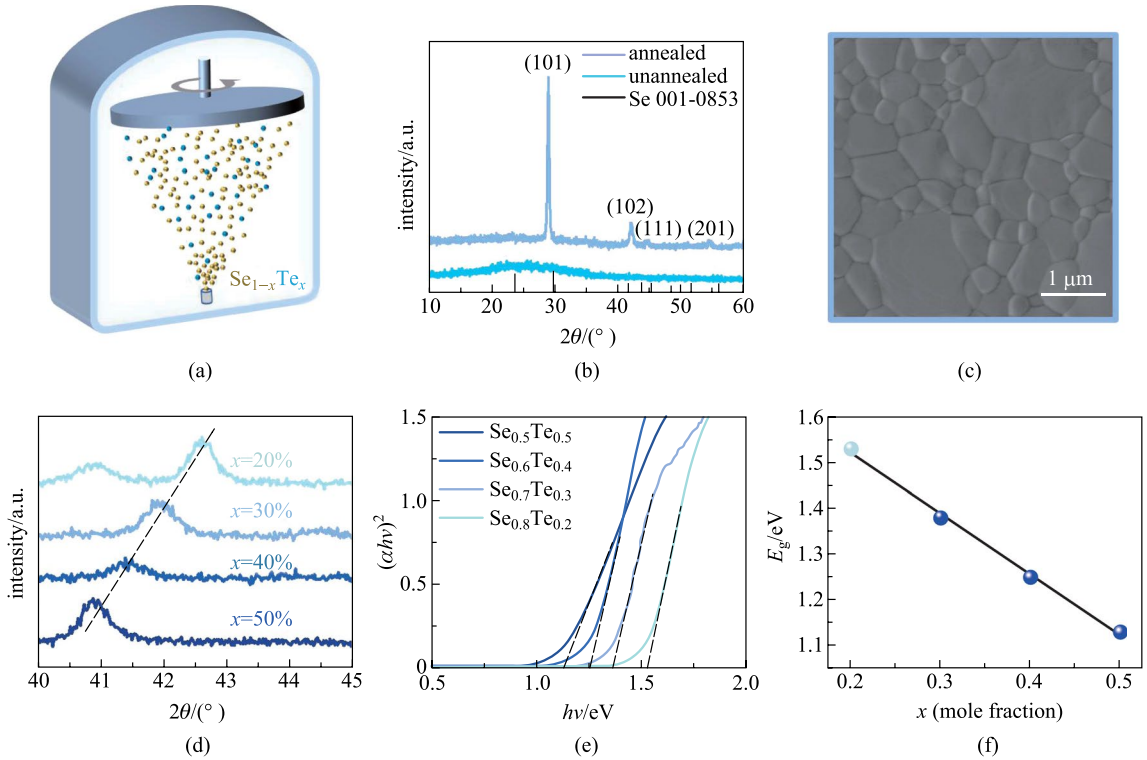

Fig. 1 **a** Schematic diagram of thermal evaporation. **b** XRD of $Se_{0.7}Te_{0.3}$ film before and after annealing. **c** SEM image of the annealed $Se_{0.7}Te_{0.3}$ film. **d** (102) diffraction peaks of $Se_{1-x}Te_x$ films. **e** Bandgaps of alloying films. **f** Bandgaps of $Se_{1-x}Te_x$ films as a function of x

high saturated vapor pressure at this temperature (Additional file 1: Fig. S3d), and the film annealed at 150 °C for 2 min is incompletely crystallized (Additional file 1: Fig. S3a). When the annealing temperature was 200 °C for 2 min, the film showed flat surface, densely arranged grains and high crystallinity (Fig. 1b, c), which meets the requirements of high-efficiency solar cells. Allowing for the high vapor pressure of Se, Se may escape from $Se_{1-x}Te_x$ films during the annealing process, giving rise to the deviation from the target component. The EDS indicated that the measured Se:(Se + Te) composition of $Se_{0.7}Te_{0.3}$ film is 0.699 (Additional file 1: Fig. S4), consistent with the feeding ratio of 0.7. Therefore, the annealing process is reasonable. Subsequently, all $Se_{1-x}Te_x$ films were crystallized at 200 °C for 2 min.

The XRD patterns of annealed $Se_{1-x}Te_x$ films with 2θ ranging from 10° to 60° are shown in Additional file 1: Fig. S2b, and the zoom-in diffraction peak of (102) is depicted in Fig. 1d. The (102) peaks shift to a small degree with the increase of x in accordance with the Bragg's Law [35] and the content of Te was calculated as expected (Additional file 1: Table S1). The morphologies of the $Se_{1-x}Te_x$ films before and after annealing were observed by AFM, which exhibits larger grains and stronger crystallinity after annealing (Additional file 1: Fig. S5). With the increase of Te content, both the grain size of $Se_{1-x}Te_x$ films, and the full width at half maxima (FWHM) of (102) peak gradually decrease (Additional file 1: Fig. S5 and Table S1). This indicates a decrease in crystallinity. The transmittance and reflectance spectra were measured on an UV–Vis spectrophotometer to determine the bandgaps of the crystallized $Se_{1-x}Te_x$ films (Additional file 1: Fig. S6). Using Tauc method [36], the bandgaps of $Se_{1-x}Te_x$ films with $x = 0.2$, 0.3, 0.4, 0.5 are fitted as 1.53, 1.36, 1.25 and 1.13 eV, respectively (Fig. 1e). The bandgap has a linear relationship with x (Fig. 1f), which well satisfies the Vegard's law (Eq. (1)) [37],

$$E_{g(Se_{1-x}Te_x)} = (1-x)E_{g(Se)} + xE_{g(Te)}, \quad (1)$$

where $E_{g(Se)} = 1.83$ eV is the bandgap of Se, and $E_{g(Te)} = 0.33$ eV is the bandgap of Te. Among them, $Se_{0.7}Te_{0.3}$ film with a bandgap of 1.36 eV has more potential according to the S–Q limit.

The position of energy levels, conduction type and carrier density are important to design the solar cell structure. Ultraviolet photoelectron spectroscopy (UPS) of $Se_{0.7}Te_{0.3}$ film demonstrated that the valence band maximum (VBM) and conduction band minimum (CBM) of the annealed $Se_{0.7}Te_{0.3}$ film are − 5.31 and − 3.95 eV, respectively (Additional file 1: Fig. S7). The detailed calculation process to obtain the VBM and CBM is shown in Additional file 1:. The positive Hall coefficient (R_H, Additional file 1:

Table S2) further confirmed that the $Se_{0.7}Te_{0.3}$ film is p-type.

An n-type ELT is needed to construct a heterojunction with p-type $Se_{0.7}Te_{0.3}$ film. Here, we selected the n-type ZnO because of its higher electron mobility and lower synthesis temperature than the commonly used TiO_2. Gibbs free energy calculation (Eq. (2), Table 1) [38] shows ZnO can slightly react with $Se_{1-x}Te_x$ during 200 °C annealing, but TiO cannot. ZnO and TiO_2 were further compared experimentally and ZnO showed a better performance as shown in Additional file 1: Fig. S8.

$$\Delta_r G_m^{\ominus}(T) = \Delta_r H_m^{\ominus}(25\,^{\circ}\mathrm{C}) - T\Delta_r S_m^{\ominus}(25\,^{\circ}\mathrm{C}), \quad (2)$$

where $\Delta_r G_m^{\ominus}$, $\Delta_r H_m^{\ominus}$ and $\Delta_r S_m^{\ominus}$ mean the changes of Gibbs free energy, enthalpy and entropy, respectively, and T is the temperature. The parameters and results of the calculation procedure are shown in Additional file 1: Tables S3 and S4 [39–41]. The existence of ZnSe is proven by the XPS measurement (Additional file 1: Fig. S9d, e). The ZnSe transition layer can enhance the adhesion between $Se_{1-x}Te_x$ and ZnO substrate and benefit the low-defectivity ZnO/$Se_{1-x}Te_x$ heterojunction interface (see Additional file 1 for experimental details). The finally designed device structure is shown in Fig. 2a, where ITO and gold with high work function are chosen as front and back electrodes, respectively.

Table 1 $\Delta_r G_m^{\ominus}$ of reactions between Se and ZnO (TiO_2) at 200 °C annealing temperature

Reaction formula	$\Delta_r G_m^{\ominus}(T)$/(kJ·mol^{-1})
$3Se(g) + 2ZnO(s) \xrightarrow{200\,^{\circ}C} 2ZnSe(s) + SeO_2(s)$	−455.78
$3Se(g) + TiO_2(s) \xrightarrow{200\,^{\circ}C} 2TiSe_2(s) + SeO_2(s)$	138.82

ZnO prepared by magnetron sputtering, shows a wide bandgap of 3.22 eV as depicted in Additional file 1: Fig. S10a, thus it does not limit the absorption efficiency of the absorber at visible band. In addition, the smooth, uniform and compact surface of ZnO (1.712 nm roughness and ~ 80 nm grain size, Additional file 1: Fig. S11) is conducive to the subsequent fabrication of $Se_{1-x}Te_x$ absorbers and gold electrodes (see Additional file 1 for detailed descriptions). The XRD of ZnO films shows that the preferred orientation is polar (111) facet (Additional file 1: Fig. S10b). According to the first-principle calculation [42], the Zn-terminal (111) facet has lower energy than the O-terminal facet. Therefore, our ZnO film is conducive to the formation of a thin Zn-Se transition layer at the interface with $Se_{1-x}Te_x$ film. Combining the energy band of ZnO [43], ZnSe [44], and $Se_{0.7}Te_{0.3}$, the band alignment is shown in Fig. 2b, which demonstrates no transport barrier for photogenerated carriers. The cross-section SEM image of the device (Fig. 2c) displays a decent interface. The thickness of ZnO and $Se_{1-x}Te_x$ were 180 and 1000 nm, respectively, but the expected ZnSe was too thin to be observed by cross-section SEM.

The device performance was characterized by a digital source meter under simulated AM 1.5G solar. The current density–voltage (J–V) curves of $Se_{1-x}Te_x$ solar cells are depicted in Additional file 1: Fig. S12a and the average and errors of efficiency are depicted in Additional file 1: Fig. S13a. As shown in Table 2, with x increases, the open-circuit voltage (V_{OC}) of $Se_{1-x}Te_x$ solar cells decreases as expected, but the short-circuit current (J_{SC}) does not always increase due to the current loss at long wavelengths according to Additional file 1: Fig. S12c. In addition, the fill factor (FF) of $Se_{1-x}Te_x$ solar cells is rather low because of the cliff at the interface and the leakage according to the small shunt resistance (R_{sh}) as shown in Additional file 1: Table S5. Then $Se_{1-x}Te_x$ solar cells with $x = 0.2$, 0.3, 0.4 and 0.5 showed

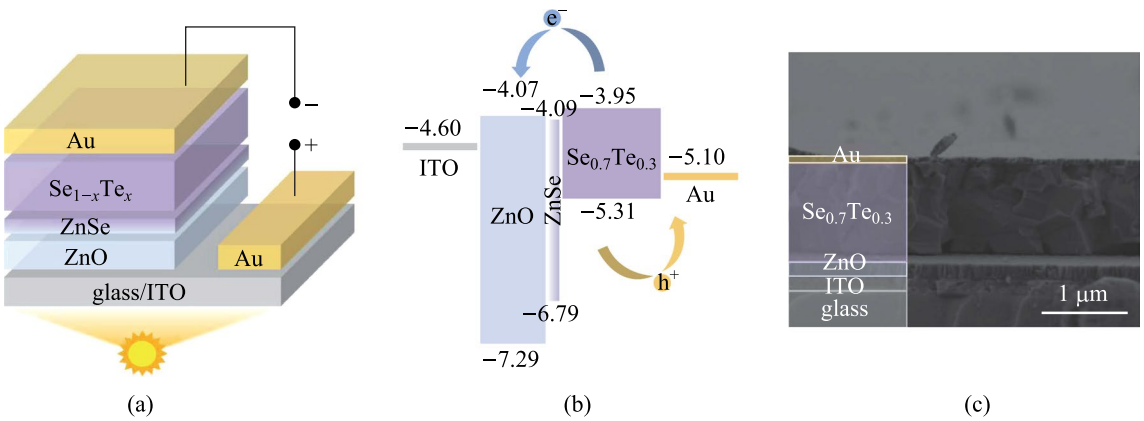

Fig. 2 **a** Structure diagram of the $Se_{0.7}Te_{0.3}$ solar cells. **b** Band alignment diagram and **c** cross-section SEM image of ITO/ZnO/$Se_{0.7}Te_{0.3}$/Au solar cells

Table 2 Device performance parameters of ZnO/$Se_{1-x}Te_x$ (x=0.2, 0.3, 0.4, 0.5) solar cells

x	V_{OC}/V	J_{SC}/(mA·cm^{-2})	FF/%	Efficiency/%
0	0.620	8.1	33.0	1.66
0.2	0.323	6.3	37.4	0.76
0.3	0.255	8.5	37.4	0.81
0.4	0.242	7.7	35.9	0.67
0.5	0.220	9.6	33.6	0.72

efficiencies of 0.76%, 0.81%, 0.67% and 0.72%, respectively (Table 2). Among them, $Se_{0.7}Te_{0.3}$ solar cell stood out with a better balance between V_{OC} and J_{SC}. Thus, we mainly focused on the $Se_{0.7}Te_{0.3}$ device and analyzed its air stability, defect properties and recombination mechanism, for the sake of providing guidance for the further performance optimization.

For the air stability, we found that the unencapsulated $Se_{0.7}Te_{0.3}$ solar cells demonstrated an improved efficiency from 0.81% to 1.25% after 1-month storage in ambient conditions (Fig. 3a and Table 3), as well as the other $Se_{1-x}Te_x$ device (Additional file 1: Figs. S12b, S13b and Table S5).

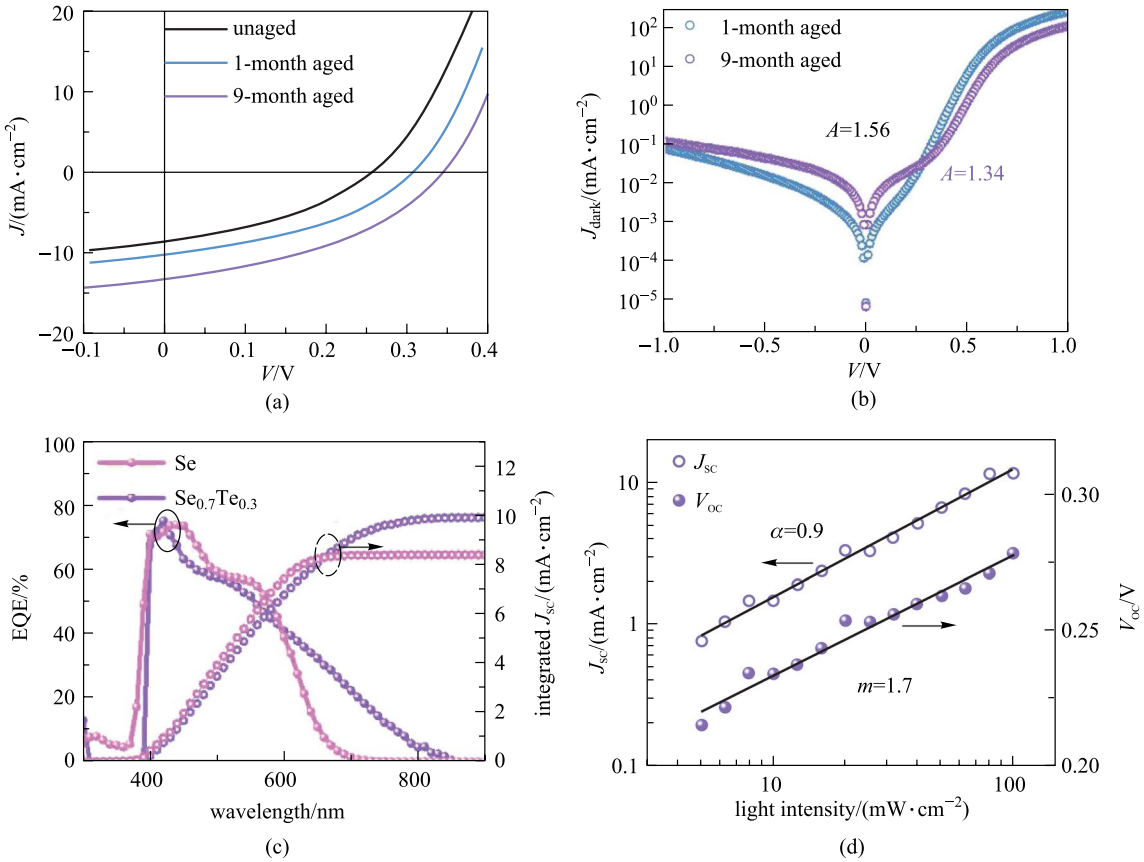

Fig. 3 **a** *J–V* curves of ZnO/$Se_{0.7}Te_{0.3}$ solar cells for different aging time under AM 1.5G solar illumination. **b** Dark *J–V* curves of ZnO/$Se_{0.7}Te_{0.3}$ solar cells after 1-month and 9-month aging. **c** EQE spectra of $Se_{0.7}Te_{0.3}$ and pure Se solar cells. **d** J_{SC} and V_{OC} curves as a function of light intensity

Table 3 Device performance parameters of ZnO/$Se_{0.7}Te_{0.3}$ solar cells for different aging times

Condition	V_{OC} /V	J_{SC} /(mA·cm^{-2})	FF /%	Efficiency /%	R_s /Ω	R_{sh} /Ω
Fresh	0.255	8.5	37.4	0.81	149	940
1-month aged	0.307	10.2	40.0	1.25	124	882
9-month aged	0.345	13.1	40.9	1.85	99	849

After 9 months, the efficiency of $Se_{0.7}Te_{0.3}$ device further increased to 1.85% (Fig. 3a and Table 3), a similar phenomenon was also observed by Todorov et al. [17]

To analyze the degree of defect recombination of aged $Se_{0.7}Te_{0.3}$ devices, the quality factor (A) fitting [45] and Hall effect measurement were conducted. By fitting the dark J–V curve [5, 46, 47], the A (1.34–1.41) of $Se_{0.7}Te_{0.3}$ device, after 9-month aging was obtained, smaller than that (1.56) after 1-month aging (Fig. 3b). Through Hall effect measurement, the carrier concentration (p) of $Se_{0.7}Te_{0.3}$ film after 1-month was 1.88×10^{14} cm^{-3} (Additional file 1: Table S2), while the p after 9-month aging was too small to be measured. The smaller A and Hall effect results illustrate the lower defect recombination (see Additional file 1 for more analysis about A). The mechanism of defect reduction in $Se_{0.7}Te_{0.3}$ film can be explained by the low diffusion barrier (0.16 eV) of Se (or Te) vacancy along Se–Se (or Te–Te) chains as shown in Additional file 1: Fig. S14 [48]. It means that the defects in $Se_{0.7}Te_{0.3}$ can reduce by the way of a self-healing process, resulting in better device performance.

Although $Se_{0.7}Te_{0.3}$ has great potential compared to Se, the device performance is inferior to the pure Se solar cells at the current stage. Inspired by Cao's work [49], a multi-junction $Se_{1-x}Te_x$-based solar cell, with the gradient distribution of the absorbers in each sub-cell to absorb the full solar spectrum, will optimize the efficiency in the future. But for now, we are focusing on the performance improvements of $Se_{1-x}Te_x$ single-junction solar cell. Therefore, a series of device physical characterizations were applied to understand the loss mechanism in our devices. According to the external quantum efficiency (EQE) spectra, the absorption edge of $Se_{0.7}Te_{0.3}$ solar cells is red shifted compared with pure Se solar cells (Fig. 3c). The full spectrum integral J_{SC} of $Se_{0.7}Te_{0.3}$ solar cells is 9.9 mA/cm^2, close to the J_{SC} from the J–V curve. However, the collection efficiency of photogenerated carriers at long wavelengths is weak, which is always attributed to the short carrier diffusion length or nonradiative recombination centers in $Se_{0.7}Te_{0.3}$ absorber. The width of the depletion region (x_d) of Se solar cells is 260 nm (Additional file 1: Fig. S15a) and the carrier diffusion length (L_d) is 480 nm (Additional file 1: Fig. S15c). Thus, the optimal thickness of Se films is 740 nm, so the absorber should be thinner to reduce the carrier recombination loss. To explore the V_{OC} loss mechanism in the $Se_{0.7}Te_{0.3}$ solar cells, we conducted the device physical characterizations to analyze the recombination loss through A and the light intensity dependent V_{OC}. The A (1–2) of the device implied that the main recombination mechanism in $Se_{0.7}Te_{0.3}$ solar cells is interface recombination. The J–V curves of the device were measured at different light intensities from 1 to 100 mW/cm^2. Figure 3d shows that the V_{OC} and logarithm light intensity have a linear relationship in accordance with Eq. (3) [50].

$$V_{OC} = \frac{mk_BT}{q}\ln I, \tag{3}$$

while the J_{SC} and light intensity satisfy the power law in accordance with Eq. (4) [50].

$$J_{SC} \propto I^{\alpha}, \tag{4}$$

where I, m, k_B, q, and α represent the light intensity, a constant, Boltzmann constant, elementary charge and logarithmic coefficient, respectively. The extracted m and α are 1.7 and 0.9, respectively. When m is larger than 1 and α is smaller than 1, the device performance is governed by the defect-related nonradiative recombination. V_{OC} deficit (defined by $(E_g - V_{OC})/q$) of $Se_{0.7}Te_{0.3}$ solar cell is 1.04 eV. It is known that the radiation recombination loss at room temperature is less than 0.3 V [51], much smaller than the real V_{OC} loss in our devices. Hence, the nonradiative recombination loss ($1.04-0.3=0.74$ eV) dominates 72% of total V_{OC} loss. To sum up, the performance of $Se_{0.7}Te_{0.3}$ device is governed by the ZnO/$Se_{0.7}Te_{0.3}$ interface recombination, and it can be minimized by interface energy band engineering or increasing the doping concentration of the absorber.

Next, we further identified the interface defect information by C–V, DLCP and AS measurement. The C–V and DLCP curves are shown in Additional file 1: Fig. S16. To acquire the defect concentration, an abrupt heterojunction model was used to fit the experimental data. The capacitance and voltage satisfied the following relationship (Eq. (5)) [52].

$$\frac{1}{C^2} = \frac{2(V_{bi} - V)}{A^2\varepsilon q N_A}, \tag{5}$$

where V_{bi}, A, ε and N_A represent for a built-in electric field, electrode area, permittivity and doping concentration, respectively. The intercept of the linear fitting (Additional file 1: Fig. S16a) on the x-axis represents the built-in potential ($V_{bi}=0.377$ V), which is close to the V_{OC} of 0.348 V. The small V_{bi} results from the small Fermi energy level difference between ZnO (−4.32 eV) and $Se_{0.7}Te_{0.3}$ (−4.73 eV). Therefore, it is important to increase the free hole density of $Se_{0.7}Te_{0.3}$ in the future. The doping density calculated through C–V and DLCP measurement are $N_{A,CV}=1.65\times10^{16}$ cm^{-3} and $N_{A,DLCP}=1.06\times10^{16}$ cm^{-3}, respectively. Interface defects can be calculated by the difference between $N_{A,DLCP}$ and $N_{A,CV}$ (Fig. 4a), the interface defect concentration of the device is 5.9×10^{15} cm^{-3}, which acts as non-radiative recombination centers, and hence affects the charge extraction. Interfacial defects may derive from interfacial Se or Te vacancies and the ZnO/$Se_{1-x}Te_x$ lattice mismatch.

Temperature dependent AS measurement was further performed to study the defect depth and defect density of state

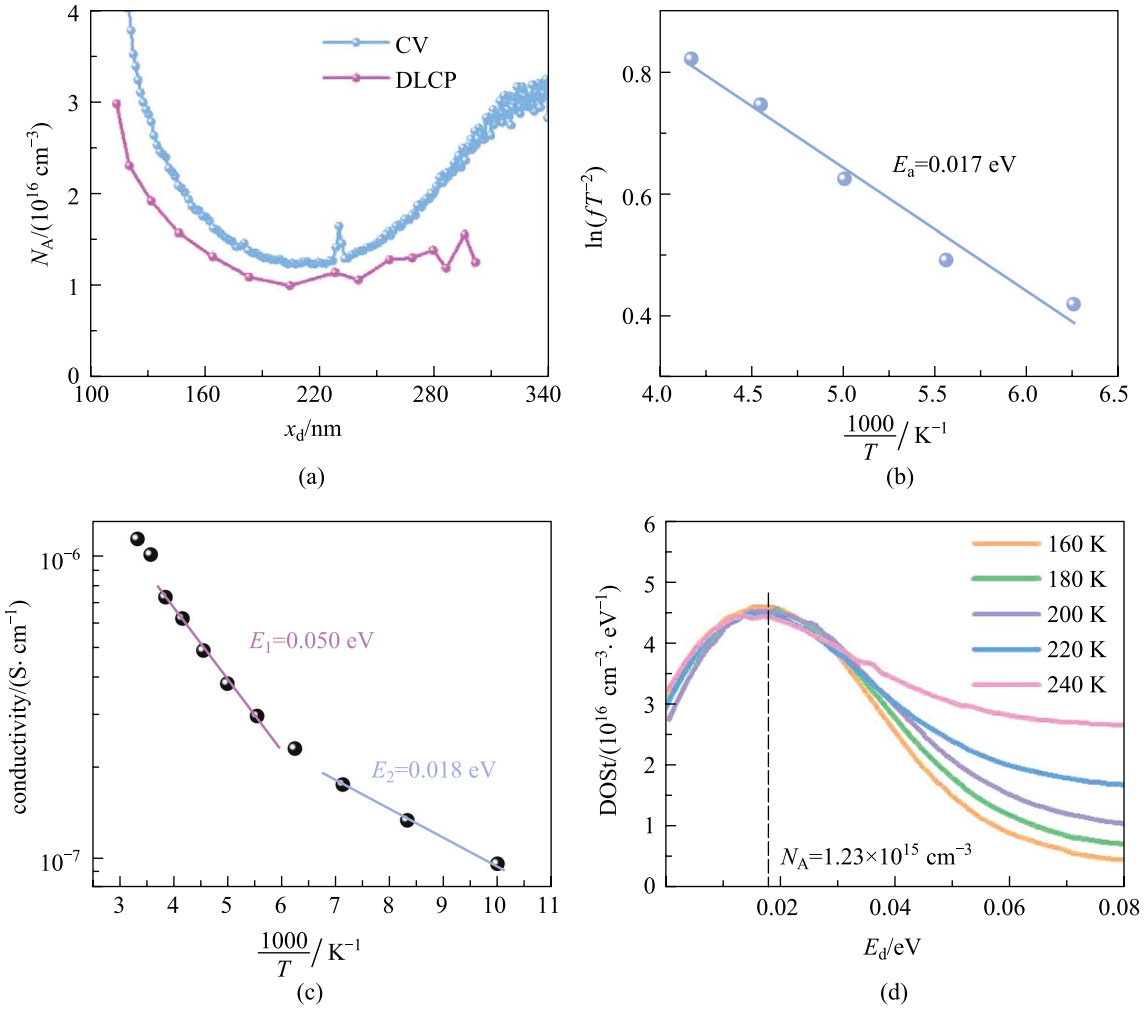

Fig. 4 **a** Relationship between N_A and x_d measured by *C–V* and DLCP. **b** Arrhenius plot. **c** Temperature dependent dark-state conductivity. **d** Defect DOSt

(DOSt). According to the AS and differential capacitance spectra (Additional file 1: Fig. S17), there is a defect signal at the frequency range from 10^2 to 10^4 Hz and at the temperature range from 180 to 240 K. The defect depth (E_d) can be calculated by Arrhenius formula (Eq. (6)) [53],

$$\ln\left(fT^{-2}\right) = -\frac{E_d}{k_B}\frac{1}{T} + \xi, \tag{6}$$

where f is the frequency, ξ is a constant without physical meaning. As shown in Fig. 4b, the fitted E_d is 0.017 eV. To further confirm defect depth obtained with AS, we measured the temperature dependent dark *I–V* curves from 80 to 320 K (Additional file 1: Fig. S18) and calculated defect depth E_a by Eq. (7) [54].

$$\sigma = \sigma_0 \exp\left(-\frac{E_a}{k_B T}\right), \tag{7}$$

where σ means conductivity and σ_0 is a constant without physical meaning. As shown in Fig. 4c, two shallow defect levels (0.050 and 0.018 eV) were observed. The shallower one was in line with E_d measured by AS, but the deeper one was not detected by AS. Combining the experimental results of temperature dependent AS and *I–V*, we inferred that there are two kinds of defect in the $Se_{0.7}Te_{0.3}$ films. Se (or Te) vacancy is easy to form, compared with the Se (or Te) interstitial defect, thus we assigned the 0.050 and 0.018 eV defects to Se and Te vacancy in $Se_{0.7}Te_{0.3}$ films, respectively.

The DOSt can be calculated by Eq. (8) [55],

$$\mathrm{DOSt}\left(E_d\right) = -\frac{V_{bi}}{q x_d}\frac{dC}{df}\frac{f}{k_B T}, \tag{8}$$

where f is the frequency and x_d is the width of depletion region. The DOSt of $Se_{0.7}Te_{0.3}$ film is shown in Fig. 4d.

The concentration by integrating the defect DOSt was 1.23×10^{15} cm^{-3}, which is two orders of magnitude higher than that of the traditional high-efficiency CdTe and $Cu_2(In,Ga)(S,Se)_2$ thin film solar cells [56]. More effort should be done to reduce the interface and bulk defects in the future.

4 Conclusion

In conclusion, ZnO/$Se_{1-x}Te_x$ solar cells were fabricated in a full vacuum environment at low temperature (less than 200 °C). We found that the Zn^{2+} exposed surface of ZnO ETL would bond with Se to form a high-quality ZnO/$Se_{1-x}Te_x$ heterojunction interface during the post-annealing process. We then tuned the bandgaps of $Se_{1-x}Te_x$ to the optimal value of S–Q limit (1.36 eV) by alloying 30% Te with 70% Se. Consequently, a superior efficiency of 1.85% was achieved based on ITO/ZnO/$Se_{0.7}Te_{0.3}$/Au device. The analysis of the recombination mechanism of the $Se_{0.7}Te_{0.3}$ device implied that the defects of ZnO/$Se_{0.7}Te_{0.3}$ interface and $Se_{0.7}Te_{0.3}$ thin film may limit the device efficiency. Our results confirmed that the construction of efficient ZnO/$Se_{0.7}Te_{0.3}$ is feasible and represented an important advance for the realization of stable, efficient and green $Se_{1-x}Te_x$ solar cells.

Supplementary Information The online version contains supplementary material available at https://doi.org/10.1007/s12200-022-00040-5.

Acknowledgements This work was supported by the National Natural Science Foundation of China (Grant Nos. 61725401, 62174064, 62105110, and 61904058), Natural Science Foundation of Hubei Province (No. 2021CFB373), Fundamental Research Funds for the Central Universities (No. 2021XXJS028), and National Key R&D Program of China (No. 2021YFA0715502). Kanghua Li thanks the support of the project funded by China Postdoctoral Science Foundation (Nos. 2020M680101 and 2021T140233). The authors acknowledge the Analytical and Testing Center of HUST and the facility support of the Center for Nanoscale Characterization and Devices (CNCD), WNLO-HUST.

Author contributions JZ carried out the film preparation, device design and performance analysis of $Se_{1-x}Te_x$ solar cells, and drafted the manuscript. JT supervised the topic selection of the manuscript, and CC supervised the writing and polishing of the manuscript. Other authors participated in the analysis and discussion of the experimental phenomena. All authors read and approved the final manuscript.

Declarations

Competing interests The authors declare that they have no competing interests.

References

1. Fritts, C.E.: On a new form of selenium cell, and some electrical discoveries made by its use. Am. J. Sci. **26**(156), 465–472 (1883)
2. Bhatnagar, A.K., Reddy, K.V., Srivastava, V.: Optical energy gap of amorphous selenium: effect of annealing. J. Appl. Phys. **18**(9), 149 (1985)
3. Tutihasi, S., Chen, I.: Optical properties and band structure of trigonal selenium. Phys. Rev. **158**(3), 623–630 (1967)
4. Dowd, J.J.: Optical properties of selenium. Proc. Phys. Soc. B **64**(9), 783–789 (1951)
5. Hegedus, S.S., Shafarman, W.N.: Thin-film solar cells: device measurements and analysis. Prog. Photovolt. Res. Appl. **12**(23), 155–176 (2004)
6. Rau, U., Werner, J.H.: Radiative efficiency limits of solar cells with lateral band-gap fluctuations. Appl. Phys. Lett. **84**(19), 3735–3737 (2004)
7. Nakamura, M., Yamaguchi, K., Kimoto, Y., Yasaki, Y., Kato, T., Sugimoto, H.: Cd-free Cu(In, Ga)(Se, S)$_2$ thin-film solar cell with record efficiency of 23.35%. IEEE Int. J. Photovolt. **9**(6), 1863–1867 (2019)
8. Yoo, J.J., Seo, G., Chua, M.R., Park, T.G., Lu, Y., Rotermund, F., Kim, Y.K., Moon, C.S., Jeon, N.J., Correa-Baena, J.P., Bulović, V., Shin, S.S., Bawendi, M.G., Seo, J.: Efficient perovskite solar cells via improved carrier management. Nature **590**(7847), 587–593 (2021)
9. Yang, G., Zhang, H., Li, S., Ren, Z., Fang, G., Lei, D., Li, G.: Enhanced efficiency and stability of triple-cation perovskite solar cells with $CsPbI_xBr_{3-x}$ QDs "surface patches". SmartMat **3**(3), 513–521 (2022)
10. Liu, Y., Dong, B., Hagfeldt, A., Luo, J., Graetzel, M.: Chemically tailored molecular surface modifiers for efficient and stable perovskite photovoltaics. SmartMat **2**(1), 33–37 (2021)
11. Romeo, A., Artegiani, E.: CdTe-based thin film solar cells: past, present and future. Energies **14**(6), 1684 (2021)
12. Brooks, L.S.: The vapor pressures of tellurium and selenium. J. Am. Chem. Soc. **74**(1), 227–229 (1952)
13. Ito, H., Oka, M., Ogino, T., Takeda, A., Mizushima, Y.: Selenium thin-film solar cell. Jpn. J. Appl. Phys. **23**(Part 1, No. 6), 719–725 (1984)
14. Nakada, T., Kunioka, A.: Efficient ITO/Se heterojunction solar cells. Jpn. J. Appl. Phys. **23**(Part 2, No. 8), 587 (1984)
15. Nakada, T., Kunioka, A.: Polycrystalline thin-film TiO_2/Se solar cells. Jpn. J. Appl. Phys. **24**(Part 2, No. 7), 536 (1985)
16. Nguyen, D.C., Tanaka, S., Nishino, H., Manabe, K., Ito, S.: 3-D solar cells by electrochemical-deposited Se layer as extremely-thin absorber and hole conducting layer on nanocrystalline TiO_2 electrode. Nanoscale Res. Lett. **8**(1), 8 (2013)
17. Todorov, T.K., Singh, S., Bishop, D.M., Gunawan, O., Lee, Y.S., Gershon, T.S., Brew, K.W., Antunez, P.D., Haight, R.: Ultrathin high band gap solar cells with improved efficiencies from the

world's oldest photovoltaic material. Nat. Commun. **8**(1), 682 (2017)
18. Tennakone, K., Kumara, G., Kottegoda, I., Perera, V., Aponsu, G.: Nanoporous n-/selenium/p-CuCNS photovoltaic cell. J. Phys. D Appl. Phys. **31**(18), 2326–2330 (1998)
19. Wang, K., Shi, Y., Zhang, H., Xing, Y., Dong, Q., Ma, T.: Selenium as a photoabsorber for inorganic-organic hybrid solar cells. Phys. Chem. Chem. Phys. **16**(42), 23316–23319 (2014)
20. Zhu, M., Hao, F., Ma, L., Song, T.B., Miller, C.E., Wasielewski, C.E., Li, X., Kanatzidis, M.G.: Solution-processed air-stable mesoscopic selenium solar cells. ACS Energy Lett. **1**(2), 469–473 (2016)
21. Green, M.A.: The path to 25% silicon solar cell efficiency: history of silicon cell evolution. Prog. Photovolt. Res. Appl. **17**(3), 183–189 (2009)
22. Green, M.A., Blakers, A.W., Shi, J., Keller, E.M., Wenham, S.R.: 19.1% efficient silicon solar cell. Appl. Phys. Lett. **44**(12), 1163–1164 (1984)
23. Anzin, V.B., Eremets, M.I., Kosichkin, Y.V., Nadezhdinskii, A.I., Shirokov, A.M.: Measurement of the energy gap in tellurium under pressure. Phys. Status Solidi A Appl. Res. **42**(1), 385–390 (1977)
24. Asendorf, R.: Space group of tellurium and selenium. J. Chem. Phys. **27**(1), 11–16 (1957)
25. Yang, P., Zha, J., Gao, G., Zheng, L., Huang, H., Xia, Y., Xu, S., Xiong, T., Zhang, Z., Yang, Z.: Growth of tellurium nanobelts on h-BN for p-type transistors with ultrahigh hole mobility. Nano-Micro Lett. **14**(1), 1–12 (2022)
26. Lin, Z., Wang, C., Chai, Y.: Emerging group-VI elemental 2D materials: preparations, properties, and device applications. Small **16**(41), 2003319 (2020)
27. Jiang, J., Meng, F., Cheng, Q., Wang, A., Chen, Y., Qiao, J., Pang, J., Xu, W., Ji, H., Zhang, Y., Zhang, Q., Wang, S., Feng, X., Gu, L., Liu, H., Han, L.: Low lattice mismatch InSe–Se vertical Van der Waals heterostructure for high-performance transistors via strong Fermi-level depinning. Small Methods **4**(8), 2000238 (2020)
28. Zhang, S., Pang, J., Cheng, Q., Yang, F., Chen, Y., Liu, Y., Li, Y., Gemming, T., Liu, X., Ibarlucea, B., Yang, J., Liu, H., Zhou, W., Cuniberti, G., Rümmeli, M.H.: High-performance electronics and optoelectronics of monolayer tungsten diselenide full film from pre-seeding strategy. InfoMat **3**(12), 1455–1469 (2021)
29. Wang, Y., Pang, J., Cheng, Q., Han, L., Li, Y., Meng, X., Ibarlucea, B., Zhao, H., Yang, F., Liu, H.: Applications of 2D-layered palladium diselenide and its van der Waals heterostructures in electronics and optoelectronics. Nano-Micro Lett. **13**(1), 1–52 (2021)
30. Hadar, I., Hu, X., Luo, Z., Dravid, V.P., Kanatzidis, M.G.: Nonlinear band gap tunability in selenium–tellurium alloys and its utilization in solar cells. ACS Energy Lett. **4**(9), 2137–2143 (2019)
31. Tan, C., Amani, M., Zhao, C., Hettick, M., Song, X., Lien, D.H., Li, H., Yeh, M., Shrestha, V.R., Crozier, K.B., Scott, M.C., Javey, A.: Evaporated Se_xTe_{1-x} thin films with tunable bandgaps for short-wave infrared photodetectors. Adv. Mater. **32**(38), 2001329 (2020)
32. Cui, S., Chahal, R., Boussard-Plédel, C., Nazabal, V., Doualan, J.L., Troles, J., Lucas, J., Bureau, B.: From selenium- to tellurium-based glass optical fibers for infrared spectroscopies. Molecules **18**(5), 5373–5388 (2013)
33. Jayah, N.A., Yahaya, H., Mahmood, M.R., Terasako, T., Yasui, K., Hashim, A.M.: High electron mobility and low carrier concentration of hydrothermally grown ZnO thin films on seeded a-plane sapphire at low temperature. Nanoscale Res. Lett. **10**(1), 7 (2015)
34. Ting, H., Ni, L., Ma, S., Ma, Y., Xiao, L., Chen, Z.: Progress in electron-transport materials in application of perovskite solar cells. Acta Phys. Sin. **64**(3), 038802 (2015)
35. Jauncey, G.E.M.: The scattering of X-rays and Bragg's law. Proc. Natl. Acad. Sci. U.S.A. **10**(2), 57–60 (1924)
36. Tauc, J.: Absorption edge and internal electric fields in amorphous semiconductors. Mater. Res. Bull. **5**(8), 721–729 (1970)
37. Denton, A.R., Ashcroft, N.W.: Vegard's law. Phys. Rev. A **43**(6), 3161–3164 (1991)
38. Carson, E.M., Watson, J.R.: Undergraduate students' understandings of entropy and Gibbs free energy. U. Chem. Ed. **6**, 4–12 (2002)
39. Dean, J.A.: Lange's Handbook of Chemistry. McGraw-Hill, New York (1999)
40. Olin, A., Olang, B.N., Osadchii, E.G., Ohman, L.O., Rosen, E.: *Chemical Thermodynamics of Selenium*, OECD Nuclear Energy Agency, France (2005)
41. Scheer, R., Schock, H.W.: Chalcogenide Photovoltaics: Physics, Technologies, and Thin Film Devices. Wiley-VCH, Baden-Württemberg, Germany (2011)
42. Parr, R.G.: Density functional theory. Annu. Rev. Phys. Chem. **34**(1), 631–656 (1983)
43. Li, M., Chen, S., Zhao, X., Xiong, K., Wang, B., Shah, U.A., Gao, L., Lan, X.Z., Zhang, J.B., Hsu, H.Y., Tang, J., Song, H.: Matching charge extraction contact for infrared PbS colloidal quantum dot solar cells. Small **18**(1), 2105495 (2022)
44. Chen, W., Zhang, N., Zhang, M.Y., Zhang, X.T., Gao, H., Wen, J.: Controllable growth of ZnO–ZnSe heterostructures for visible-light photocatalysis. CrystEngComm **16**(6), 1201–1206 (2014)
45. Gokmen, T., Gunawan, O., Mitzi, D.B.: Minority carrier diffusion length extraction in $Cu_2ZnSn(Se, S)_4$ solar cells. J. Appl. Phys. **114**(11), 114511 (2013)
46. Sites, J.R., Mauk, P.H.: Diode quality factor determination for thin-film solar cells. Solar cells **27**(1), 411-417 (1989)
47. Sites, J.R.: Quantification of losses in thin-film polycrystalline solar cells. Sol. Energy Mater. Sol. Cells **75**(1–2), 243–251 (2003)
48. Liu, Y., Wu, W., Goddard, W.A., 3rd.: Tellurium: fast electrical and atomic transport along the weak interaction direction. J. Am. Chem. Soc. **140**(2), 550–553 (2018)
49. Cao, Y., Zhu, X., Tong, X., Zhou, J., Ni, J., Zhang, J., Pang, J.: Ultrathin microcrystalline hydrogenated Si/Ge alloyed tandem solar cells towards full solar spectrum conversion. Front. Chem. Sci. Eng. **14**(6), 997–1005 (2020)
50. Liao, W., Zhao, D., Yu, Y., Grice, C.R., Wang, C., Cimaroli, A.J., Schulz, P., Meng, W., Zhu, K., Xiong, R.G., Yan, Y.: Lead-free inverted planar formamidinium tin triiodide perovskite solar cells achieving power conversion efficiencies up to 6.22. Adv. Mater. **28**(42), 9333–9340 (2016)
51. Shockley, W., Queisser, H.: Detailed balance limit of efficiency of *p-n* junction solar cells. J. Appl. Phys. **32**(3), 510–519 (1961)
52. Abou-Ras, D., Kirchartz, T., Rau, U.: Advanced Characterization Techniques for Thin Film Solar Cells. Wiley-VCH, Germany (2016)
53. Proskuryakov, Y.Y., Durose, K., Taele, B.M., Welch, G.P., Oelting, S.: Admittance spectroscopy of CdTe/CdS solar cells subjected to varied nitric-phosphoric etching conditions. J. Appl. Phys. **101**(1), 014505 (2007)
54. Seto, J.Y.W.: The electrical properties of polycrystalline silicon films. J. Appl. Phys. **46**(12), 5247–5254 (1975)
55. Walter, T., Herberholz, R., Müller, C., Schock, H.W.: Determination of defect distributions from admittance measurements and application to Cu(In, Ga)Se_2 based heterojunctions. J. Appl. Phys. **80**(8), 4411–4420 (1996)
56. McCandless, B.E., Buchanan, W.A., Thompson, C.P., Sriramagiri, G., Lovelett, R.J., Duenow, J., Albin, D., Jensen, S., Colegrove, E., Moseley, J., Moutinho, H., Harvey, S., Al-Jassim, M., Metzger, W.K.: Overcoming carrier concentration limits in polycrystalline CdTe thin films with in situ doping. Sci. Rep. **8**(1), 14519 (2018)

Jiajia Zheng received her Bachelor's degree from Nanchang University (China) in 2019. She is currently pursuing her M.S. degree from both the Huazhong University of Science and Technology (HUST, China) and the Mines ParisTech University (France). She majors in New Energy Science and Technology in China-EU Institute for Clean and Renewable Energy in HUST. Her current research interests focus on thin-film solar cells and photodetectors.

Liuchong Fu received his Bachelor's degree from Huazhong University of Science and Technology (China) in 2020. He will receive his master's degree of Optical Engineering from Wuhan National Laboratory for Optoelectronics at Huazhong University of Science and Technology (China) in 2023.06. His research interests are photovoltaics and photodetectors.

Yuming He received his Bachelor's degree from Huazhong University of Science and Technology (China) in 2021. He is currently a master, major in Electronic Information at School of Optical and Electronic Information, Huazhong University of Science and Technology (China). His research interests are thin-film solar cells and infrared detectors.

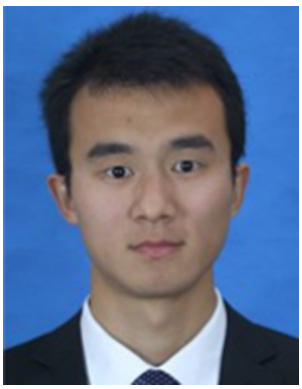

Kanghua Li received his Bachelor's degree from Huazhong University of Science and Technology, China in 2015. Then he studied in Wuhan National Laboratory for Optoelectronics, Huazhong University of Science and Technology as a doctoral candidate and received his Ph.D. degree in 2020. Currently, he is a post-doctor in Wuhan National Laboratory for Optoelectronics at Huazhong University of Science and Technology, China. His research interests are thin-film solar cells and photodetectors.

Yue Lu received his Bachelor's degree from China University of Geosciences (Wuhan), China in 2019. He is currently pursuing his M.S. degree from both Huazhong University of Science and Technology (China) and the Mines ParisTech University (France). He majors in New Energy Science and Technology in China-EU Institute for Clean and Renewable Energy in HUST. His current research interests focus on thin-film solar cells and photodetectors.

Jiayou Xue received his Bachelor's degree from University of Jinan (China). He is currently a candidate for a Master's degree at Huazhong University of science and technology and Mines ParisTech University (France). He majors in Clean and Renewable Energy China-EU Institute for Clean and Renewable Energy in HUST. His current research interests focus on photovoltaic cells.

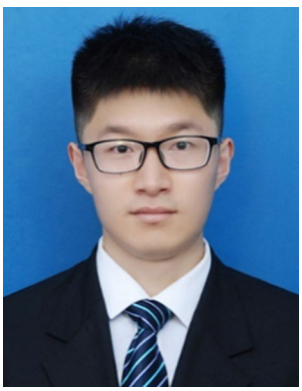

Yuxuan Liu received his Bachelor's degree from Hefei University of Technology (China). He is currently a candidate for a Doctoral Degree at Huazhong University of science and technology. His major is Optical Engineering at Wuhan National Laboratory for Optoelectronics. His research interests are quantum dot infrared detectors.

Chong Dong received her Bachelor's and Master's degrees from Soochow University (China). She is currently a candidate for a Doctoral Degree at Huazhong University of science and technology. Her major is Electronic Science and Technology at Wuhan National Laboratory for Optoelectronics. Her research interests are quantum dot infrared detectors.

Chao Chen received his B.S. degree in School of Physics at Huazhong University of Science and Technology (HUST), China in 2014. From 2014/09 to 2019/02, he studied in Wuhan National Laboratory for Optoelectronics at HUST as a doctoral candidate and received his Ph.D. degree in 2019. From 2019/02 to 2021/02, he worked in Wuhan National Laboratory for Optoelectronics as a post-doctor. Recently, he joined School of Optical and Electronic Information, HUST as an associate professor. His research interests are thin-film solar cells and photodetectors.

Jiang Tang is a professor at Wuhan National Laboratory for Optoelectronics, Huazhong University of Science and Technology, China. He obtained his Ph.D. degree from University of Toronto, Canada in 2010. His research interest is optoelectronic devices including X-ray and infrared detectors, thin-film solar cells, and light-emitting diodes. He has published > 150 papers, filed > 30 patents.